International Journal of Advanced Manufacturing Technology, Volume 107, April 2020, pp. 3093-3107
DOI: 10.1007/s00170-020-05214-z

An experimental study on lap joining of multiple sheets of aluminium alloy (AA 5754) using friction stir spot welding

Danka Labus Zlatanovic[a*], Sebastian Balos[a], Jean Pierre Bergmann[b], Tobias Köhler[b], Michael Grätzel[b], Leposava Sidjanin[a] and Saurav Goel[c,d]

[a] Department of Production Engineering, Faculty of Technical Science, University of Novi Sad, Novi Sad, Serbia

[b] Department of Production Technology, Ilmenau University of Technology, Ilmenau, Germany

[c] School of Engineering, London South Bank University, 103 Borough Road, London SE1 0AA, UK

[d] School of Aerospace, Transport and Manufacturing, Cranfield University, Bedford MK43 0AL, UK.

Corresponding author Email ID: danlabus@uns.ac.rs and GoeLs@Lsbu.ac.uk

Abstract

Friction stir spot welding (FSSW) process is widely used in the automobile industry for a range of applications such as battery components, standard wire connectors and terminals. This manuscript addresses two grand challenges in the arena of FSSW, hitherto, unaddressed in the extant literature: (i) lap joining of thin sheets (0.3 mm thickness) of AA 5754 alloy and (ii) lap joining of more than two sheets using FSSW. To accomplish this task, a novel pinless convex shaped tool was designed to alter the stress state while gradually advancing the tool which led to achieving stress state necessary for obtaining defect free lap joints. The weld joints were inspected by optical microscopy, SEM imaging and analysed by nanoindentation tests and Vickers microindentation tests for assessment of the quality of the weld interface (WI). Process parameters of FSSW such as torque on the tool and axially applied load were used to analytically obtain the average local measure of peak normal and axial stresses as well as the coefficient of friction in the contact zone. In samples welded at low rotational speeds, strain-hardening mechanism was seen dominating in contrast to samples welded at higher rotational

speeds, which showed thermal softening. As a direct consequence of this, the samples welded at low rotational speeds showed much higher hardness at the weld surface than the samples welded at higher speeds. A strong transition of strain hardening to thermal softening was noticeable beyond an applied strain rate of 400 s^{-1}.

Key words: friction stir spot welding; convex pinless tool; multiple sheets; thin sheet; 5754 H-111 aluminium alloy, strain hardening, thermal softening

Abbreviations:

CDRX	**Continuous dynamic recrystallisation**
CoF	**Coefficient of friction**
CFSW	**Conventional friction stir welding**
CFSSW	**Conventional friction stir spot welding**
DS-FSW	**Double-side friction stir welding**
EDS	**Energy dispersive spectroscopy analysis**
FE-SEM	**Field emission scanning electron microscope**
FFSSW	**Flat friction stir spot welding**
FSC	**Friction stir channelling**
FSP	**Friction stir processing**
FSR	**Friction stir riveting**
FSS	**Friction stir surfacing**
FSBR	**Friction stir blind riveting**
FSCl	**Friction surface cladding**
FSIF	**Friction stir incremental forming HD**
FSSVW	**Friction stir spot vibration welding**
FSSW	**Friction stir spot welding**
FSW	**Friction stir welding**
HAZ	**Heat affected zone**
HD	**Hook defects**
HFSC	**Hybrid friction stir channelling**
IL-FSSW	**Intermediate layer friction stir spot welding**
In-situ SPM	**In-situ scanning probe microscopy**
MFSC	**Modified friction stir channelling**
RFSSW	**Refill friction stir spot welding**
RPM	**Revolutions per minute**
RSW	**Resistance spot welding**
PFSSW	**Protrusion friction stir spot welding**
PLC	**Portevin-Le Chatelier effect**
PLT-FSSW	**Friction stir spot welding with pin-less tool**
SADP	**Selected area diffraction pattern**
SEM	**Scanning electron microscope**
SFSSW	**Swing friction stir spot welding**
SFSW	**Submerged friction stir welding**
SPM	**Scanning probe microscopy**
SR-FSW	**Self-reacting (bobbin) stir welding**
SZ	**Stir zone**
TMAZ	**Thermomechanical affected zone**
TWI	**The welding institute**
USW	**Ultrasonic spot welding**
WFSSW	**Walking friction stir spot welding**
WI	**Welded interface**
µFSW	**micro friction stir welding**

1.0. Introduction

The substitution of copper (8.96 g/cm^3) by aluminium (2.7 g/cm^3) is being sought as an immediate engineering requirement for battery components, strand-terminal connectors and terminals to save weight and transportation costs. However, an issue that appears in the literature is the successful and reliable joining of aluminium alloy sheets. Therefore, the development of joining technologies for aluminium alloys, with acceptable weld characteristics and minimal energy consumption are emerging rapidly [1–3].

Currently, the most frequently used spot joining techniques for assembling aluminium alloy sheets are resistance spot welding (RSW) [4], cold metal transfer spot welding [5], laser spot welding [6], ultrasonic spot welding (USW) [7], self-piercing riveting [8] and friction stir spot welding (FSSW) [2]. In contrast to other technologies, FSSW consumes low energy and because of being a solid-state welding process, it can provide superior mechanical properties to the processed material compared to the base material. Hence, there lies a considerable incentive for research on this topic.

Friction stir welding (FSW) is the technique which was developed at The Welding Institute (TWI) of the UK in 1991 [9]. Initially, it was applied only to welding but over the years, the technique has gained popularity for use in surface property enhancement, channelling, riveting, forming and many more other processes. A series of developments in the field have led to the emergence of a latitude of processes that are all based on harnessing the principal of friction stir processing. Fig. 1shows an attempt to classify and summarise these friction-based manufacturing processes by consolidating the literature available on this topic.

Conventional FSSW is a solid-state welding technique that was developed by the German research center GKSS. Mazda was among the first companies to report first application of FSSW for lap joining during mass production of its 2003 RX-8 cars [2, 10].

FSSW technique relies on plunging a rotational tool (consisting of a pin and a shoulder) into the overlapping area of the two sheets until the shoulder of the tool touches the surface of the upper sheet. Thereafter, the tool is retracted and leaves a keyhole behind [11–14]. The keyhole represents the

biggest drawback of the conventional FSSW process. It has been shown that the keyhole reduces the effective cross section area of the joint, which adversely affects the mechanical properties of the joint [15] and this becomes the potential site for corrosion [16, 17]. Two methods were proposed to fill the keyhole, refill friction stir welding (RFSSW) [18–21] and intermediate layer friction stir welding (IL-FSW) [22], but both RFSSW and IL-FSW demand complicated equipment. The most common problems known to occur in all types of FSSW joints are hook defects (HD). It is shown by the researchers that HDs occur during IL-FSSW [23] and RFSSW [24] and they tend to reduce the weld joint strength.

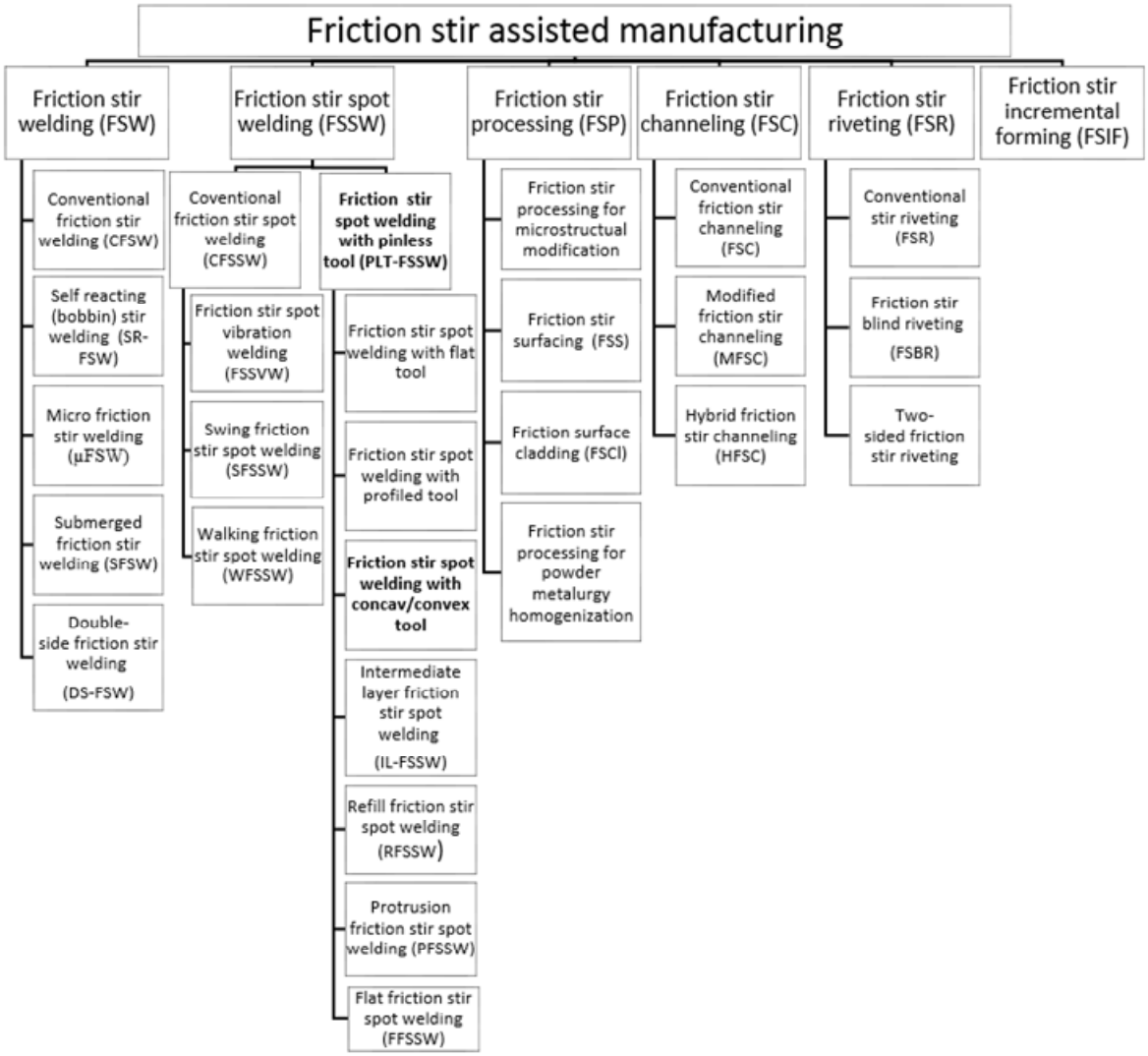

Fig. 1 Classification of the friction stir assisted manufacturing processes

Bakavos *et al.* [25] studied FSSW of 0.93 mm thick aluminium copper alloy, with a flat pin-less tool

(Ø 10 mm) with five different surface features and cycle (welding) time varying from 0.5-2.5 s. High lap shear strength (~3.4 kN) was achieved, however, different types of defects like HDs, flashes, circumferential shear crack and unwelded and/or partially bonded weld joints were observed. Pinless FSSW offers a better alternative to overcome the aforementioned problems as the joining during this process is assisted by dynamic recrystallisation and diffusion bonding between the two layers [26]. Both mechanisms occur above the temperature of recrystallisation. However, diffusion prevails under the influence of high axial stress while dynamic recrystallisation is driven by high shear stresses in the contact zone. State-of-the-art concerning the topic of FSSW suggests that despite some success, it has not been possible to use FSSW to fabricate sheets of thickness less than 0.93 mm. Moreover, the literature on this topic lacks evidence on whether more than two sheets were welded at a time, so it has been assumed here that joining multiple thin sheets is an ongoing challenge. After identifying the knowledge gaps discussed above, several key questions emerged that will be addressed as part of this research effort:

(a) Can the pinless FSSW method be used to lap join multiple sheets of thickness as low as 0.3 mm?
(b) If yes, what should be an ideal tool geometry of the pinless tool to achieve this task?
(c) What is the influence of rotational speed of the tool on the microstructure of the weld shape and properties of the weld joint?
(d) Whether the pinless FSSW process is dominated by strain hardening or thermal softening and what magnitude of strain rate governs these two mechanisms?

The above questions motivated the design and development of a new tool in this work with a geometry capable of welding multiple thin sheets of a softer aluminium alloy. The overarching motivation of this paper stems from the fundamental curiosity of studying the allied process characteristics of the pinless FSSW process by complete characterisation of the mechanical properties to achieve a defect free weld joint.

2.0. Equipment and materials

2.1. Base material – Aluminium alloy 5754-H111

Samples used for FSSW were cut from thin sheets of rolled commercial aluminium alloy 5754-H111 (AlMg3) of dimensions 44 mm x 50 mm x 0.3 mm. **Error! Reference source not found.** provides details of the chemical composition of the base material *(*aluminium alloy 5754-H111*)* that was measured using an optical emission spectrometer *(*ARL 3580*)*. Prior to welding, the base material was mechanically tested for its uniaxial stress-strain property using a Hegewald & Peschke Inspect Retrofit universal testing machine. The tensile stress-strain curve obtained for the base material is shown in Fig. 2 and in light of the experimental results discussed in the later part of the paper, this plot was used to draw a sound comparison with the analytical stress analysis obtained from the data.

Table 1 Chemical composition of AA 5754-H111 aluminium alloy

Element	Si	Fe	Cu	Mn	Mg	Cr	Zn	Ti	Al
Wt%	0.19	0.24	0.03	0.30	3.10	0.03	0.005	0.014	bal.

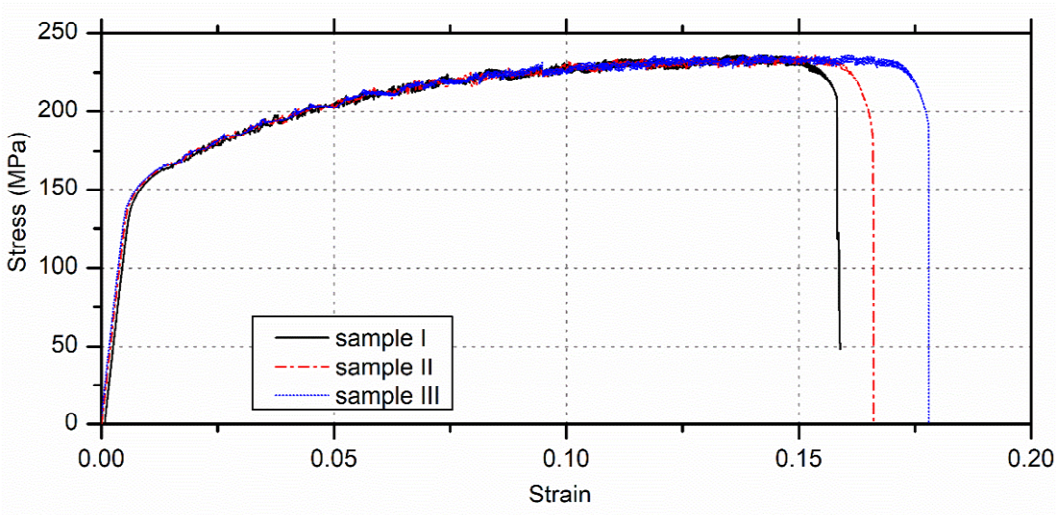

Fig. 2 Stress-strain curve of the base material AA5754 alloy (the test was repeated three times showing the peak deformation stress remains unchanged)

2.2. Equipment

2.2.1. Working principle

Fig. 3 (a) illustrates the experimental scheme and Fig. 3 (b) shows the tool geometry that was used to lap join four thin sheets during this work. The tool was produced in the lab using H13 (X40CrMoV5-1) hot-work tool steel with its material chemical composition shown in Table 2.

Table 2 Chemical composition of H13 tool steel (X40CrMoV51) from the supplier data sheet

Element	C	Cr	Mb	V	Fe
Wt.%	0.4	5.1	1.35	1.1	bal.

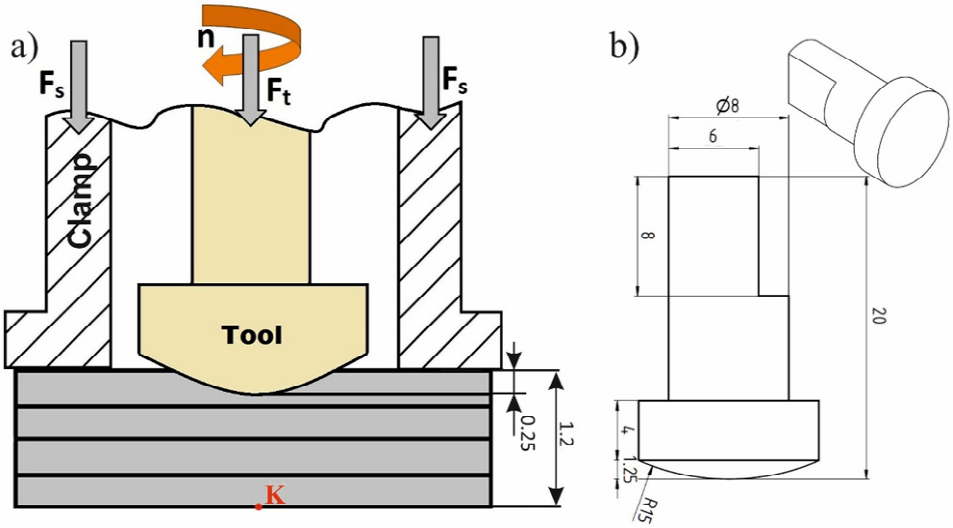

Fig. 3 a) FSSW tool setup (F- force on the tool) and b) details of tool geometry

The welding system consist of a clamping system (used to constrain the material during FSSW) movable in the vertical direction, providing sample clamping as shown in Fig. 3(a). The way this machine works is that the sample is firstly held by the clamping system and during this time, the preloaded tool starts to come vertically downwards onto the upper sheet. The tool rotation initiates as soon as the system detects the tool touch onto the surface of the upper sheet. The time in which the tool completes its operation (cycle time) depends on the resistance of the material (soft materials are easily displaced), applied axial load, rotational speed and the total tool travel distance. Upon reaching its target vertical displacement, the tool retracts quickly. During the FSSW process, a K-type thermocouple (Fig. 3) was placed at the center of the bottom of the substrate with a view to gaining information on the variation in temperature during the different runs carried out at different rotational speeds.

2.2.2. Proposed convex tool design considerations

After a series of dummy trials, it was found that the traditional flat pinless tool did not work for joining multiple thin sheets. As opposed to a flat tool which causes tearing of sheets (highlighted in red circles in figure 4) due to a large contact radius, a convex tool presents a gradually increasing contact radius as a function of the depth of tool engagement providing a better contact condition between the tool and sheets.

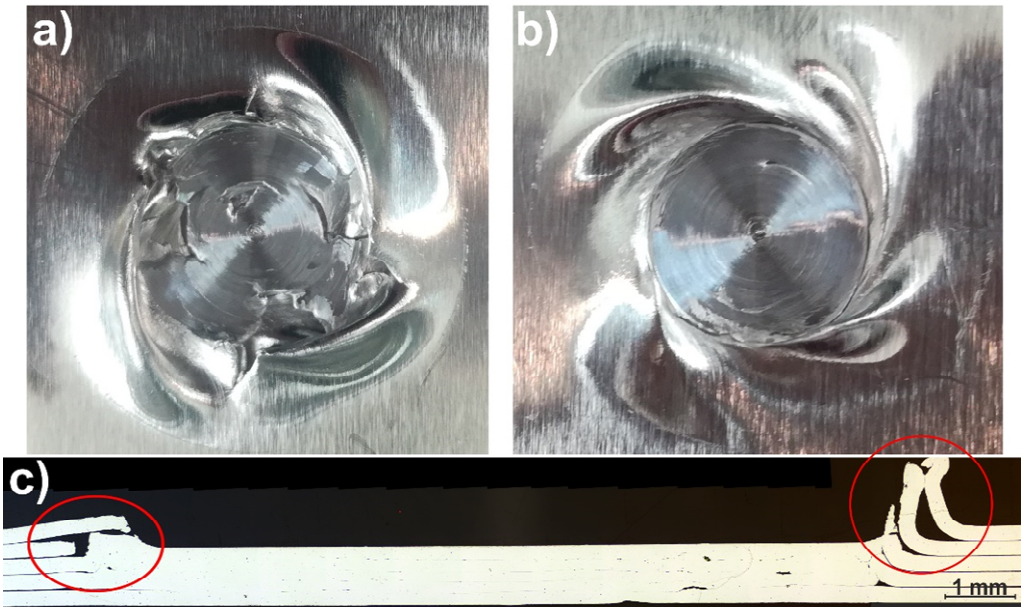

Fig. 4 Macrographs of two samples (a, b) and cross-section view of the sample from figure (b) welded with flat tool of diameter 10 mm *(*five sheets of 0**.**2 mm thickness) welded at (a) 2000 RPM, 0.2 mm plunge depth and 5 kN axial force and (b) with 2000 RPM, 0**.**2 mm plunge depth and 2 kN axial force) red circles show tarred edges of the first two sheets after welding with flat tool geometry.

To produce a high-strength multilayer weld joint using the pinless tool, it is necessary to produce a certain level of stress to arouse material flow, that is, to generate conditions for dynamic recrystallisation as well as diffusion between the two interfaces [9]. During FSSW, the material flow is most pronounced at the maximal contact radius of the tool where the angular velocity of the tool is maximum. However, at the center of the tool, the angular velocity is theoretically zero. In this small area, the material is compressed due to the axial pressure present in the contact zone causing an individual grain to yield and with an increased penetration, resulting in dislodging of the adjacent grain. In a nutshell, this means that a flat tool creates a uniform pressure along the entire radius of the tool, and it is unsuitable for welding multiple aluminium thin sheets in FSSW. On the other hand, a convex tool by virtue of a

gradually changing contact radius causes the shear stress to grow gradually as a function of contact depth. From what became clear out of this work, the convex angle (the slope presented by the tool) will have a marked influence on the cycle (welding) time and it remains an area of future work to compare convex tools with different slopes to optimise the tool geometry for performing FSSW.

2.3. Process parameters

FSSW experiments were carried out on an adapted force controlled EJOWELD C50R FSSW machine which is designed to run at rotational speed of up to 9000 RPM, maximum axial load of 8 kN and maximum cycle time of 5 s. To start the process, the tool was made to contact the surface of the top sheet to be welded and then it was rotated along the axis normal to the sheet surface at a fixed RPM. A predefined constant load was applied to achieve the desired contact depth (usually less than the thickness of the upper sheet).

During the experiments, the tool experienced an upward normal force termed as axial load which was maintained at 2 kN throughout the experiments reported in this work. The axial displacement made by the tool at this load (often referred as 'plunge depth') was maintained at 0.25 mm in all the experiments. During the trials, rotational speed was varied in increments of 500 RPM ranging from 1500 RPM to 3500 RPM as shown in Table 3 Experimental FSSW parameters.

Table 3 Experimental FSSW parameters used in the work

Sample	Rotational speed (RPM)	Axial load (kN)	Plunge depth (mm)	Cycle time (s)
RW1-1	1500	2	0.25	4.95
RW1-2				4.7
RW1-3				4.3
RW2-1	2000	2	0.25	4.93
RW2-2				4.87
RW2-3				4.18
RW3-1	2500	2	0.25	4.82
RW3-2				4.29
RW3-3				4.12
RW4-1	3000	2	0.25	4.43
RW4-2				3.99
RW4-3				4.45
RW5-1	3500	2	0.25	3.92
RW5-2				3.57
RW5-3				3.83

The focus of experiments was to collect the experimental data at five rotational speeds of 1500, 2000, 2500, 3000 and 3500 RPM. Each experiment was repeated three times and an average reading was used to report the results in this work.

2.4. Material characterisation of the welded joints

After FSSW, the metallographic examinations were performed. As for this, the welded joints were ground with sandpaper (grit 360 to 2500) and polished with diamond suspensions (6 and 3 µm). The final polishing step was done with 0.05 µm colloidal silica. Electrolytical etching was done on Struers LectroPol-5 equipment (40 V, 2 min, Barkers etchant). The cross-sectional morphology of the joints was analysed by a light microscope (Zeiss AxioScope.A1 with AxioCam ICc3) for etched samples and a Zeiss Axio Vert.A1 MAT with AxioCam 105 with crossed polarised light and sensitive tint was used to analyse polished samples. Further characterisation of samples was carried out using the Field Emission Scanning Electron Microscope (FE-SEM) (Hitachi S-4800)**.**

2.5. Mechanical testing of welded joints

2.5.1. Microhardness mapping using Vickers tests

As for the evaluation of the local variation in mechanical properties, microhardness imaging of the weld joints was obtained using standard Vickers microhardness tests (Struers DuraScan 70 machine) at a load of 0.1 kg. Fig. 5 shows an illustrative scheme that was implmented to program the machine to obtain the cross-section hardness imaging of the welded specimens. The interspacing of 0.33 mm between the indented points ensured that there was little or no reflection of stress waves induced in the material during each indent cycle.

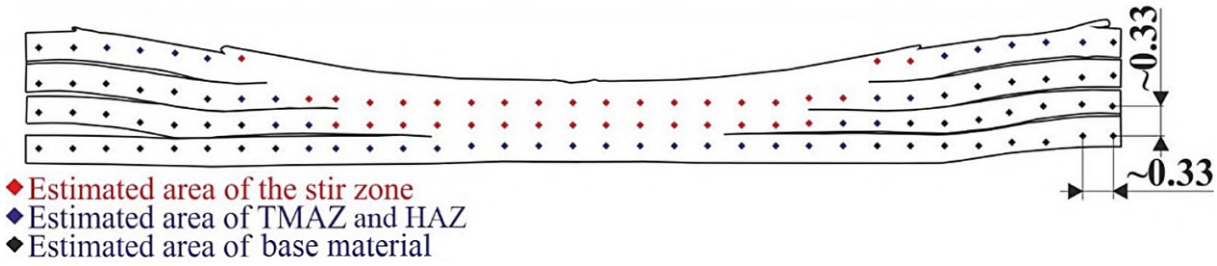

Fig. 5 Schematic illustration of microhardness mapping. All measurements are in mm

2.5.2. In-situ Scanning Probe Microscopy (in-situ SPM) using Hysitron Nanoindentation

Beside Vickers test, a more refined nanomechanical hardness mapping and testing was made using scanning probe microscopy (SPM) with an instrument from Bruker Hysitron XPM (TI 980 Nanoindenter) equipped with a Berkovich tip. The XPM load function was set to be 20 × 20 indents, 500 nm separation and 150 µN peak load. Almost about 400 indents were performed in about 3 minutes. A sample result shown in Fig. 6 (a) marked with a red square (in the joint interface) highlights a small area (25 µm × 25 µm) mapped by hardness testing while the welding was performed at 1500 RPM. A fully automated testing was performed on both sides of the weld faying interface (WFI) and measurements were stitched to obtain a mapped image shown in Fig. 6 (b).

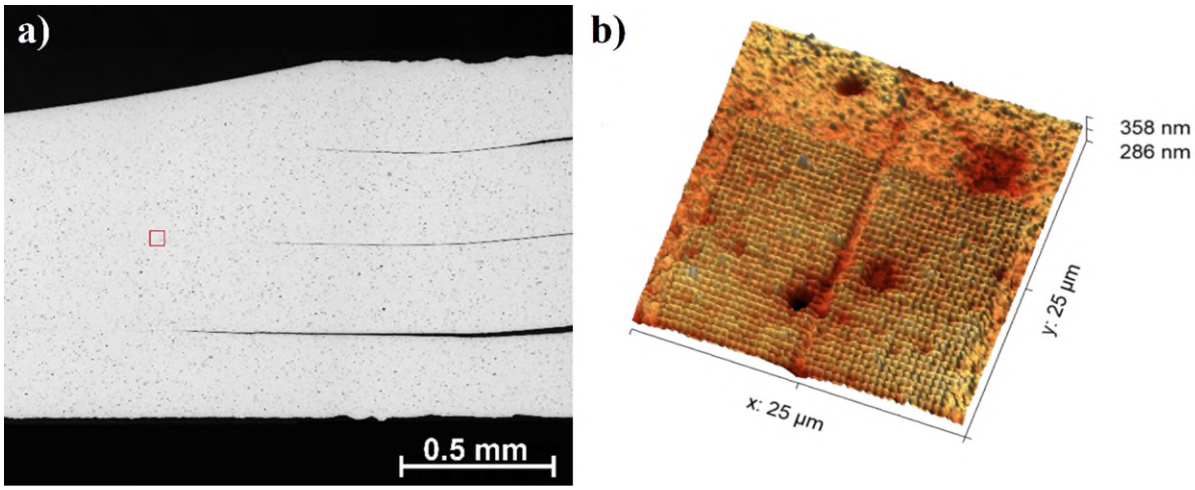

Fig. 6 (a) Sample welded at 1500 RPM showing an area marked for nanoindentation analysis; (b) indented array

3.0. Results and discussions

3.1. Stress analysis, hardness mapping and microstructural variation in the welded zone

The apparatus used to perform FSSW was equipped to provide the measurements of torque (N·m) and cycle (welding) time (s), while the temperature (°C) information at the bottom of the sample was obtained via thermocouple as explained earlier via Fig. 3. Post-processing of the data was carried out

by using analytical formulae shown below to estimate the coefficient of friction, axial stress and shear stress in the contact[27, 28].

$$\tau(t) = \frac{2 \cdot T(t)}{\pi \cdot r(t)^3} \quad (1)$$

$$\sigma_n(t) = \frac{F(t)}{r(t)^2 \cdot \pi} \quad (2)$$

$$\mu(t) = \frac{\tau}{\sigma_n} = \frac{2 \cdot T(t)}{F(t) \cdot r(t)} \quad (3)$$

where, R is the fixed tool radius (mm) and $r(t)$ is the instantaneous contact radius $r(t) = \frac{\sqrt{4 \cdot R^2 - (2 \cdot R - 2 \cdot h)^2}}{2}$ (mm) calculated from the data of axial displacement of the tool (plunge depth) (mm) h(t) , $F(t)$ is the applied axial load measured during the process (N), $T(t)$ is the torque (N·mm). $\sigma_n(t)$ and $\tau(t)$ refer to axial and shear stresses (MPa) respectively and μ (t) is the coefficient of friction. At the beginning of the operation, the axial load was set to be 2 kN.

Fig. 7 shows the evolution of two major stresses $\sigma_n(t)$ and $\tau(t)$ in the welded zone, namely the axial stress presented by the virtue of applied axial load and the shear stress estimated from the torque data presented by the virtue of tool rotation. During early stages of the contact, it is primarily the axial stress that helps the tool to plunge into the workpiece surface and this gives rise to the stick type of contact conditions between the tool and the workpiece.

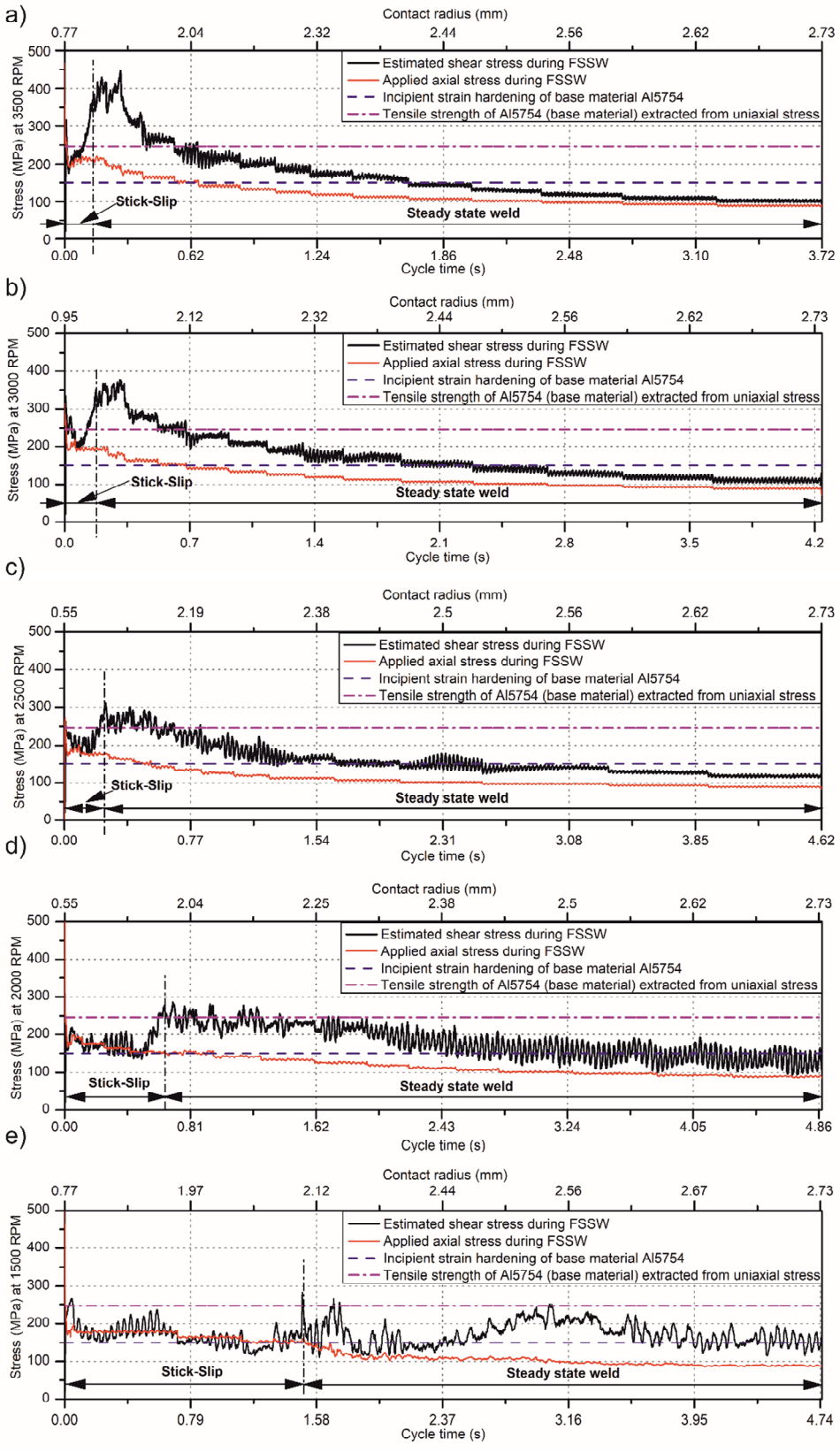

Fig. 7 (a) to **(e)** Evolution of applied axial stress and shear stress over time estimated from the applied load and torque data at different RPMs starting from 1500 RPM to 3500 RPM**.** The plots are also compared against the yield limits and tensile strength of Al 5754 base metal obtained from the tensile stress-strain data of AA 5754

As Fig. 7shows, the increasing penetration of the tool vertically downward (specifically for the convex tool) cause the magnitude of shear stress to rise and it scales linearly (seen by a sudden sharp increase). At higher speeds, slip dominates sticking and the competition between these two stress states influences the residual stress state on the welded surface. Moreover, a steady state welding condition was obtained after the competing stick-slip conditions stablised the tool-workpiece contact. Particularly noteworthy from the stress profiles is that during the early stages of contact, the axially applied stress dominates the shear stress as the area of contact between the tool and workpiece is relatively smaller. It means that before a certain threshold area activates, the contact between the tool and workpiece did not achieve a steady state for the plastic flow of the material, particularly until the slip (shear stress) does not start to dominate over the stick (axial stress). Reilly *et al.* [29] simulated the material flow phenomena during FSSW process. A close inspection of their simulations and the experiments performed in this work indicates that during the initial stages of the contact, the centripetal velocity drags the material inwards underneath the tool. It can analogously be understood or seen by visualising the pathline of a particle at an imaginary radius (outer periphery) 'x' such that the particle at the peripheral radius of 'x' is pulled in a spiral net inward and underneath the tool. This portion of material trapped between the tool and workpiece continues to churn under the rotational action of the tool with increasing downward displacement of the tool. The shear stress during this time tries to overcome the work of displacing this portion of material from radius 'x' to inside of the core. As this portion of the material deforms, the shear stress goes up before eventually reducing down. This point signifies the transition from unsteady tool-workpiece contact to a steady contact such that the shear stress beyond this point decreases almost monotonically as evident from Fig. 7.

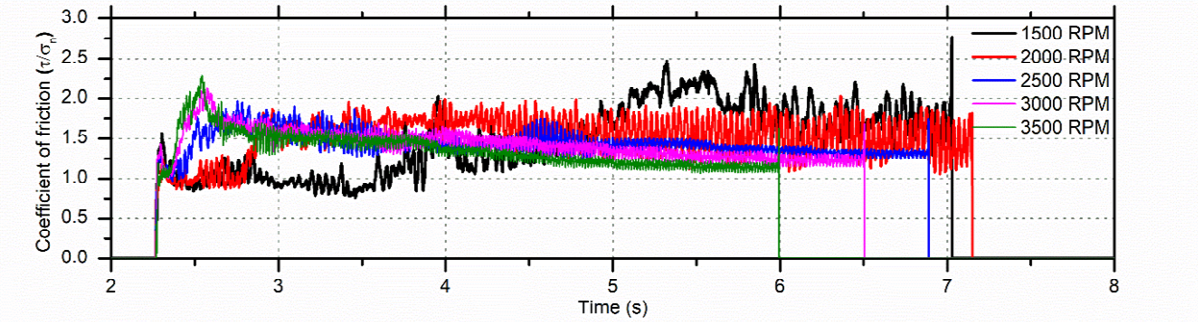

Fig. 8 Variation in the coefficient of friction (CoF)

Fig. 8 shows variation in the coefficient of friction at five rotational speeds of FSSW examined in this work. The value of CoF vary between 1 and 2.5 depending on the speed of operation. A higher value of CoF at the end of the process was observed to be responsible for strain hardening of the surface (e.g. 1500 RPM) where CoF was about 1.75 at the end of operation as opposed to the lower value of CoF of 1.14 at the start of the process. Farhat *et al.*[30] and Kumar *et al.*[31] reported that FSW process at low rotational speeds (from 200 to 1400 RPM) is governed by strain hardening.

The phenomena of strain hardening at low RPMs was also verified by examining the Vickers hardness imaging (shown in Fig. 9) revealing that the microhardness on the surface was highest in the welded zone for samples welded at low speeds. Overall, in samples welded at 1500 RPM and 2000 RPM, the strain hardening mechanism dominates over thermal softening and conversely in samples welded at 3000 and 3500 RPM thermal softening was more pronounced.

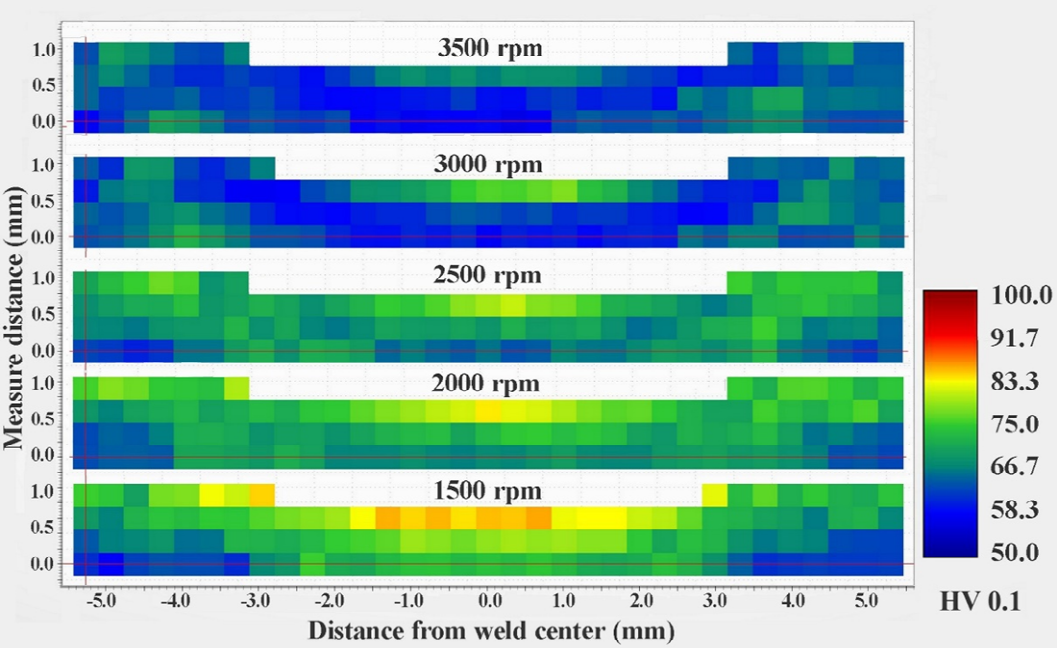

Fig. 9 Microhardness maps obtained by Vickers test revealing cross-sectional hardness of all samples processed by FSSW at RPM's ranging from 1500 to 3500 RPM

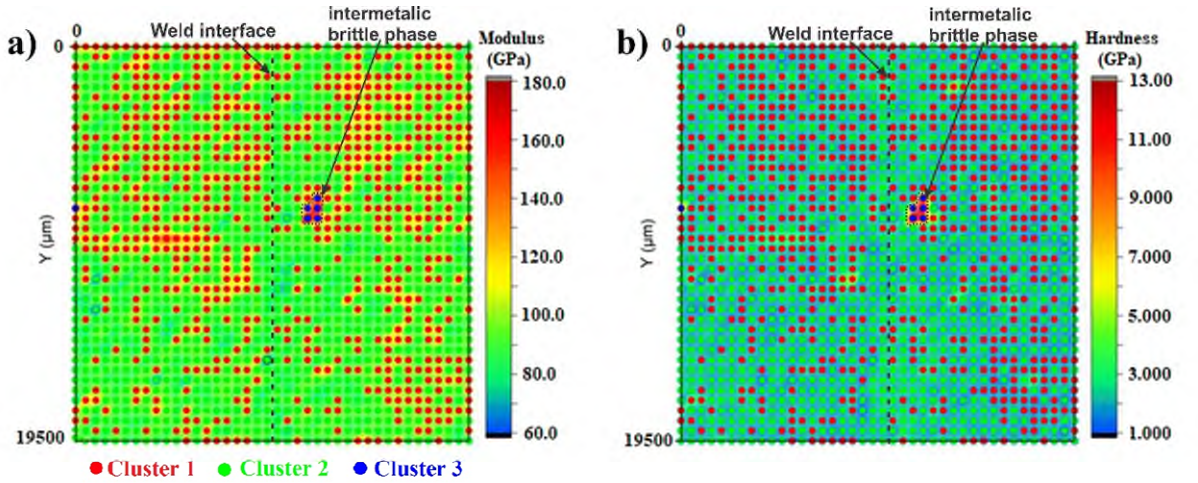

Fig. 10 Elastic modulus and hardness map of the welded zone at low RPM of 1500. The figure was obtained using **K-means clustering** method to obtain (a) Young's modulus and (b) nanohardness maps

Table 4 Values of the modulus and hardness organised in three clusters (blue>red>green) showing the average values of the clusters obtained from the maps from **Error! Reference source not found.**

Statistic	Cluster 1 Modulus (GPa)	Cluster 1 Hardness (GPa)	Cluster 2 Modulus (GPa)	Cluster 2 Hardness (GPa)	Cluster 3 Modulus (GPa)	Cluster 3 Hardness (GPa)
Mean	103.37	**2.1186**	88.248	**1.8692**	154.62	**10.23**
Standard deviation	6.6549	0.33693	5.8924	0.22696	16.259	1.9906
Standard error	0.25117	0.012716	0.19729	0.0075993	6.6377	0.81266
Number of points	702	702	892	892	6	6
Variance	44.287	0.11352	34.72	0.051513	264.35	3.9625
Skewness	1.7829	3.8779	-1.0754	-0.52025	0.416	-0.10107
Kurtosis	5.2635	29.374	1.4843	0.94858	-1.1111	-0.79584

To augment support to the argument about strain hardening mechanism revealed by Vickers tests, nanoindentation was used for further analysis of strain-hardened region. Fig. 10in conjunction with Table 4shows three different clusters (marked in red, green and blue) in strain hardened region revealing variations in hardness and elastic modulus probed by the nanoindentation mapping. From a quantitative analysis, the first and second cluster seems to correspond to strain hardened material in the stir zone) while the third cluster (appears discretely and barely very few in numbers) showing highest values appears to be intermetallic brittle phase of AA 5754 alloy.

It is noteworthy that the samples welded at 1500 and 2000 RPM showed a serrated stress-time curve (jerky flow) seen earlier inFig. 7. According to Yamada *et al.* [32] the appearance of jerky flow signifies that the solute Mg atoms as well as precipitates in Al – Mg alloy interacts with dislocations. This phenomenon is known as Portevin - Le Chatelier (PLC) effect. Materials like Al-Mg alloys possess the tendency to exhibit PLC effect while they undergo inhomogeneous plastic deformation. Furthermore, under conditions of local increase of the strain rate above certain limit leads to softening of the material locally. Next, the formula proposed by Chang et al. [33] was used to perform caculations for estimating the applied strain rate as a function of rotational speed.

$$\dot{\varepsilon} = \frac{R_m \cdot 2 \cdot \pi \cdot r_e}{L_e} \quad (4)$$

where r_e and L_c are the effective (average) radius and depth of the stir zone (recrystallised zone) measured with the help of ImageJ software from cross- sections of etched samples. Chang *et al.* [33] estimated average material flow *Rm* to be half of the tool rotation speed.

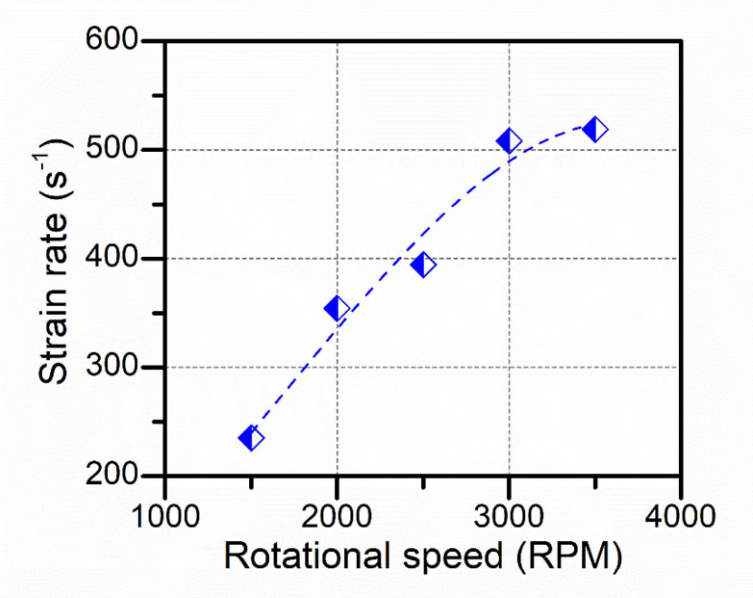

Fig. 11 Relation between tool rotational speed and strain rate

Gerlich *et al.* [34] estimated strain rate at different rotational speeds (from 750 to 3000 RPMs) in Al 5754 CFSSW samples by using Zener -Holloman parameter and obtained strain rate vs. rotational speed curve close to the curves presented in this paper. It can be seen that during FSSW, the strain rate increases with increasing rotational speed. According to stress-cycle time plots, CoF vs. time

plots and hardness measurements, it can be concluded that strain hardening is more pronounced at strain rates lower than 400 s^{-1} and thermal softening is more pronounced at strain rates >400 s^{-1}.

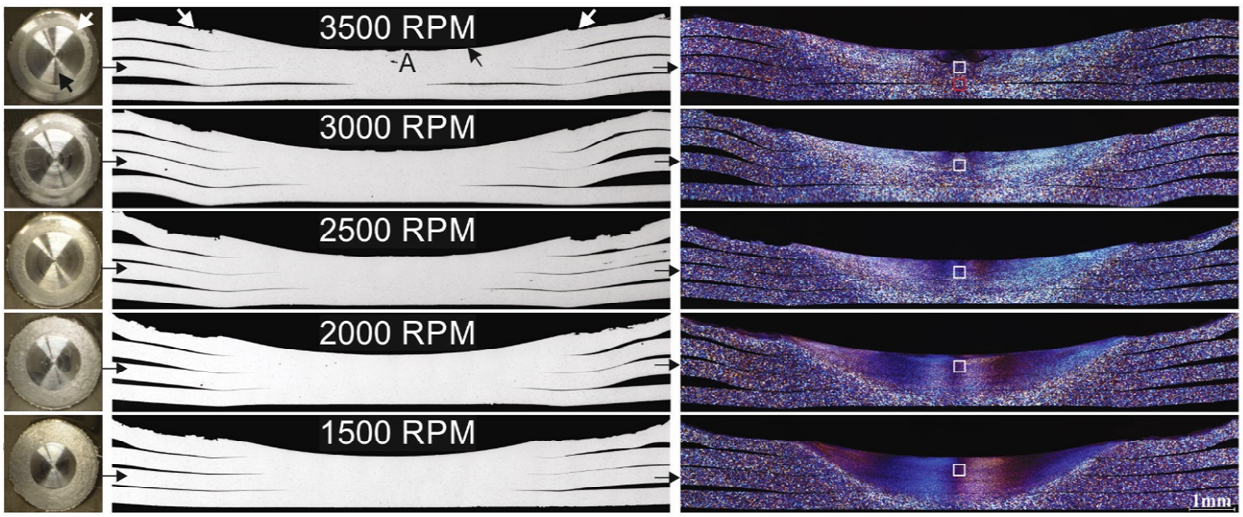

Fig. 12 Macrographs and cross-section view of the welded joints at different RPM

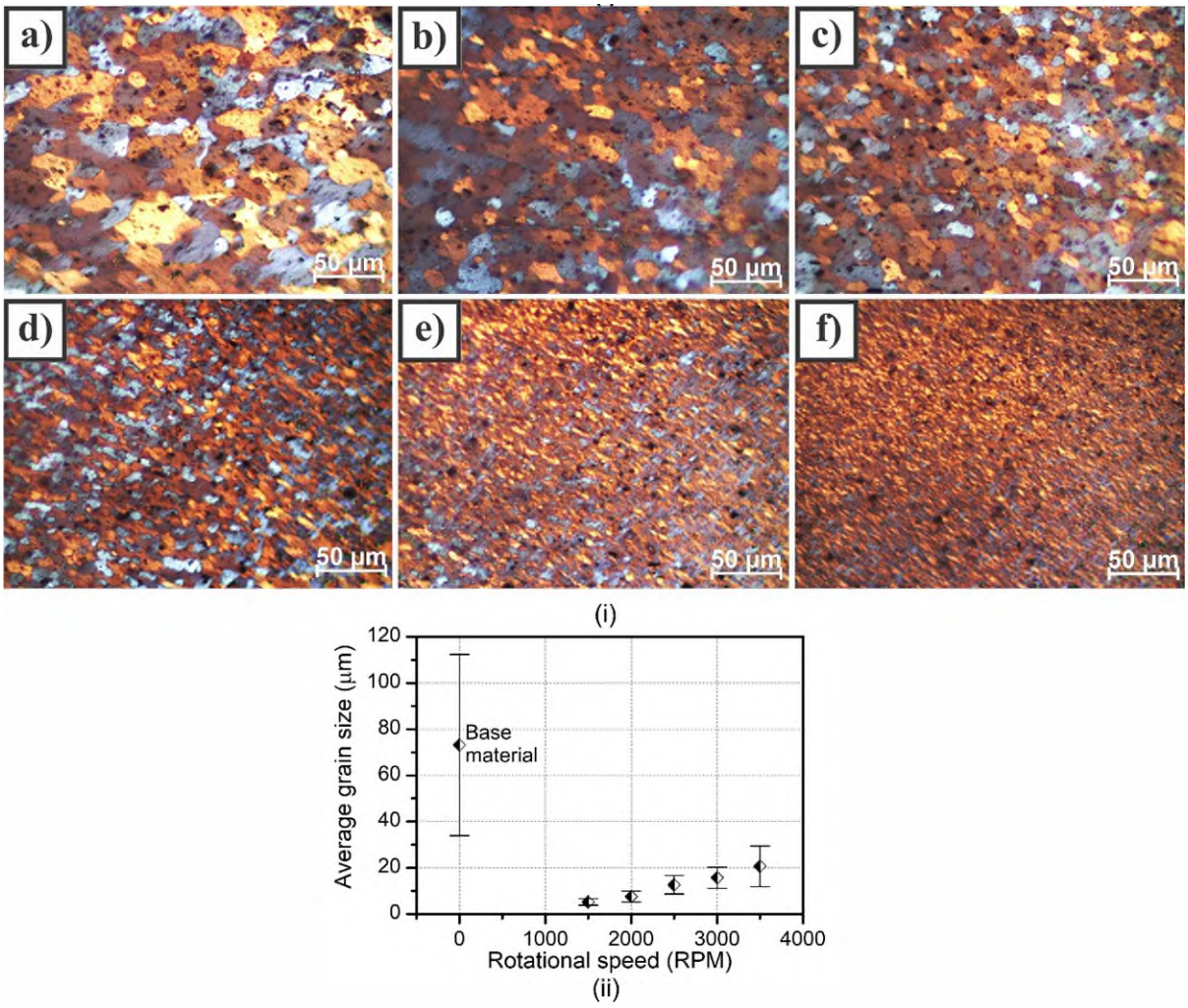

Fig. 13 (i) Cross-section light microscopy images (white squares in (i)) showing grain microstructure of: a) base material; b) welded sample with 3500 RPM; c) with 3000 RPM; d) with 2500 RPM; e) with 2000 RPM and f) with 1500 RPM revealed by Barkers etchant and (ii) average grain size measured for different rotational speeds and base material with standard deviation

To lend credence to this observation, the grain size conditions were assessed by subjecting the cross-section of the welded zones to electrolytical etching. The variations in the grain size are shown in Fig. 12 and Fig. 13 respectively. It is clear that a low RPM (low strain rate < 400 s^{-1}) leads to small grain sizes while high RPM (strain rate > 400 s^{-1}) leads to coarser grains. Jata *et al.* [35] proposed continuous dynamic recrystallization (CDRX) as grain refinement mechanism during FSSW. This process is driven by temperature, strain and strain rate as well as interaction between precipitates and solute atoms with dislocations. In few texts, [21, 35–37], it was revealed that the magnitude of misorientation angle increases significantly during FSSW/FSW compared to the base material. Thus, new grains seen in the stir zone can be disorientated subgrains. Repeated dislocations absorption into subgrain boundaries is

the dominating mechanism during CDRX for increasing the misorientation angle between adjacent subgrains [9]. Therefore, it is proposed that the microstructure in samples welded at different rotational speeds is influenced by (i) grain size reduction by subgrain rotation induced by dislocation glide and (ii) subgrain coarsening where average subgrain size increase while number of subgrain decreases and which is driven by the reduction of local misorientation associated with intracrystalline recovery. The former is more dominating in samples where strain hardening overcomes thermal softening (lower rotational speeds) while the latter is more dominating in samples where thermal softening is more pronounced.

3.2. *Characteristics of the weld joint shape*

Error! Reference source not found. shows an outcome of the entire FSSW process revealing detailed nature and shape of the welded joint interface.

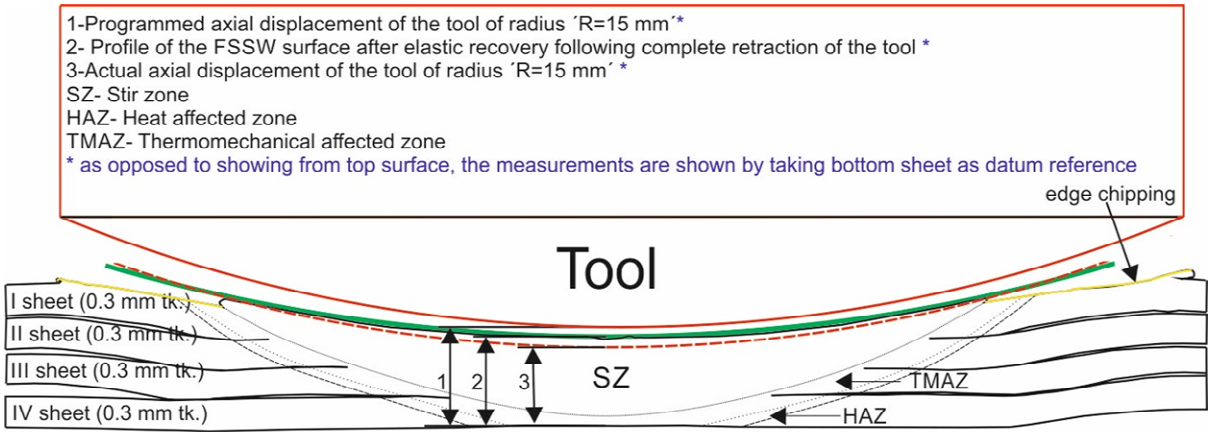

Fig. 14 Schematic illustration of the FSSW process observed in this work summarizing the presence of stir zone, heat affected zone, thermomechanical affected zone and elastic recovery of the surface after the release of pressure by withdrawal of the tool

Of importance to note from figure 14 is the presence of edge chipping on the outer periphery of the contact radius. The examination of this cross-section reveals a strong presence of fracture as opposed to plastic deformation (white arrows) in Fig. 12 at 3500 RPM. It is clear that the sheets on the outer side of clamping tends to go upward during FSSW but are constrained by the clamping system. Consequently, there are opposite thermal stresses developed radially (σ_r) in the sheet. Due to continued downward movement of the tool, this radial stress grows further and results in material going upwards

(although stochastically) to come in contact with the tool. The portion of sheet material that comes in contact with the tool is smeared away and leaves behind the sites of fracture. Earlier it was shown that the edge chipping [38] contours are rather complex and shows no regularity. Also, the parameter "fractal mean square deviation" is quite useful in evaluation of this contour profile. What is apparently clear though is that when the magnitude of tensile stress goes past a certain threshold value exceeding the fracture toughness of the metal, it causes chipping rather than plastic deformation as evident in this work.

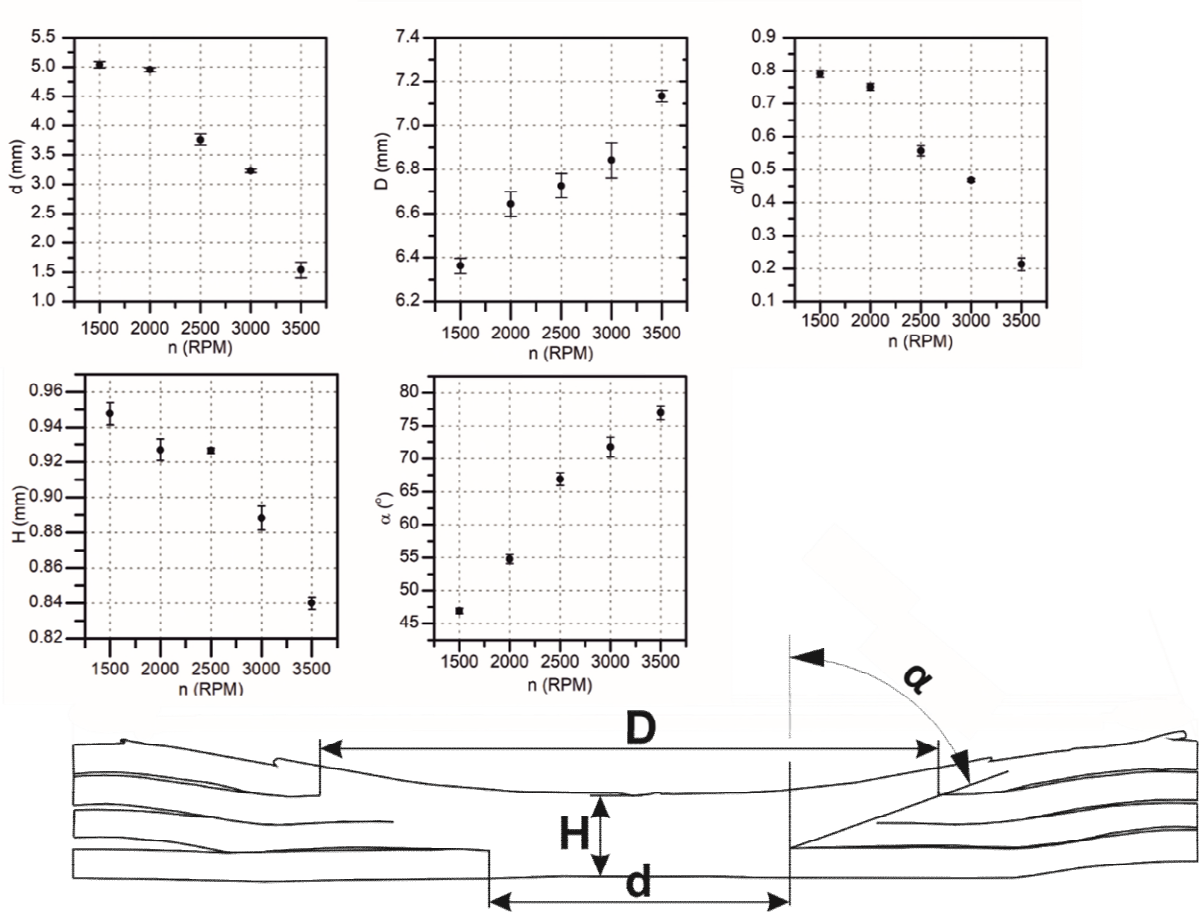

d: Bottom diameter of the stir zone
D: Top diameter of stir zone
H: Axial depth of the stir zone
α: Taper angle of the stir zone

Fig. 15 Dimensional quantification of the weld characteristics measured as a function of rotational speed of the tool

Fig. 15 shows variations in several physical parameters measured as a function of rotational speed of the tool. Those parameters include for instance the measurement of d (bottom diameter of the stir zone), D (top diameter of the stir zone), H (axial height of the stir zone), and α (taper angle of the stir zone). After a careful data analysis, it became clear that the actual advancement of FSSW tool into the workpiece during the process appears to be consistently higher than the programmed depth of advancement (shown in Fig. 15as inverted from the bottom). This could be attributed either to the positioning errors or to material induced plastic effects in the stir zone (contributing to different viscosity and permeability of material for the tool to go past) that impedes the sensor from precisely detecting the surface of the sheet, which was being considered as the theoretical datum for measurement reference.

Most notably, it was observed that an increase in the rotational tool speed led to an increase in the *D* parameter. It simply means that a higher RPM produces samples with conical shape and taper angle 'α'.The taper angle 'α' decreases linearly with a decrease of rotational speed of the tool, leading to an almost cilindrical shape of stir zone in samples welded at 1500 RPM.

The parameter d/D ratio was observed to decrease with an increase of rotational speed. The ratio of 1 would make the shape to be cylindrical. During steady state weld, the axial load applied on the workpiece pushes the softened material up and lacks sufficient stress in lower part of the sample, which causes *D* to increase while *d* and *H* decreases. As rotational speed increases, the cycle time decreases but the temperature increases (see Fig. 16) causing thermal softening of the material.

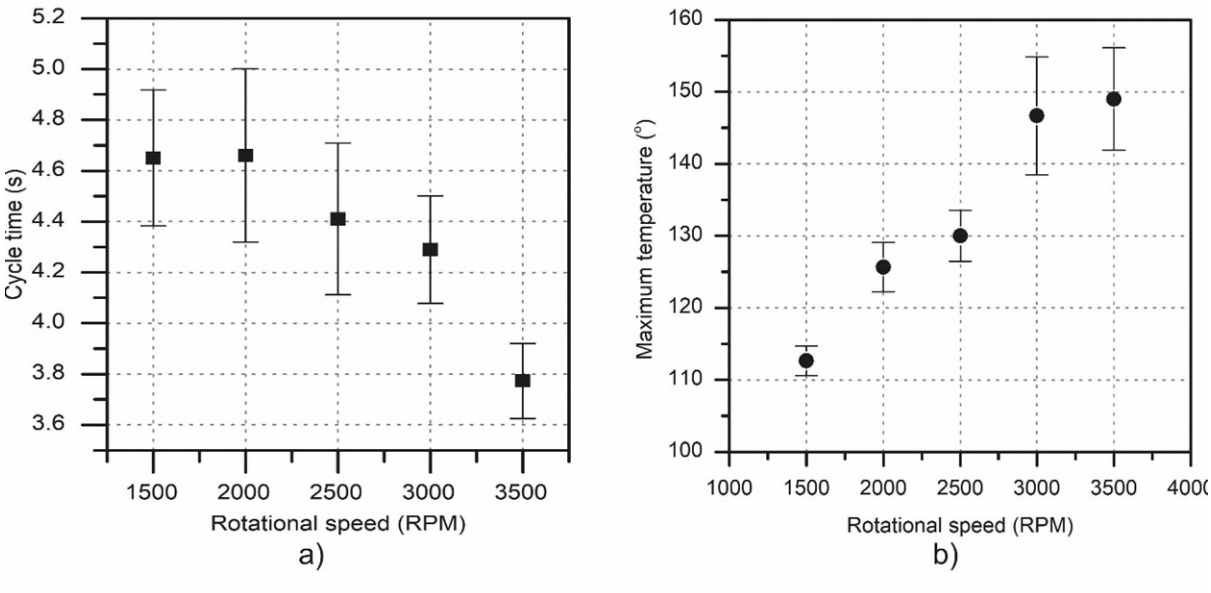

Fig. 16 (a) Cycle time, and (b) temperature variation as a function of the rotational speed

Usually during FSSW the presence hook defects, wormhole or partially bonded areas are presented as major type of defects in the weld joints [39–41]. However, the scarcity of literature on FSSW of sheets of thickness less than 0.93 mm does not confirm this andit is possible that the hook defects appear only above some critical thickness.

To analyse this, SEM inspection of the weld interface was made as shown in Fig. 17. Fig. 17 corresponds to the same locations as shown in Fig. 12(a) with white and red squares for bonded regions between the first (uppermost) and second sheets and between the third and fourth respectively. It was observed that (a), a fully bonded region was obtained which did not show any obvious boundary at the interfacing surfaces, whereas in some other regions, as shown in Fig. 17(b) showed few partially bonded regions characterised by intermittent welded areas and intermittently present interfacial boundaries were noticed especially pronounced at higher rotational speeds. The samples welded at 3500 RPM were found to have occasional wormhole defect near to the center of the sample and the last two sheets were observed to be only partially bonded.

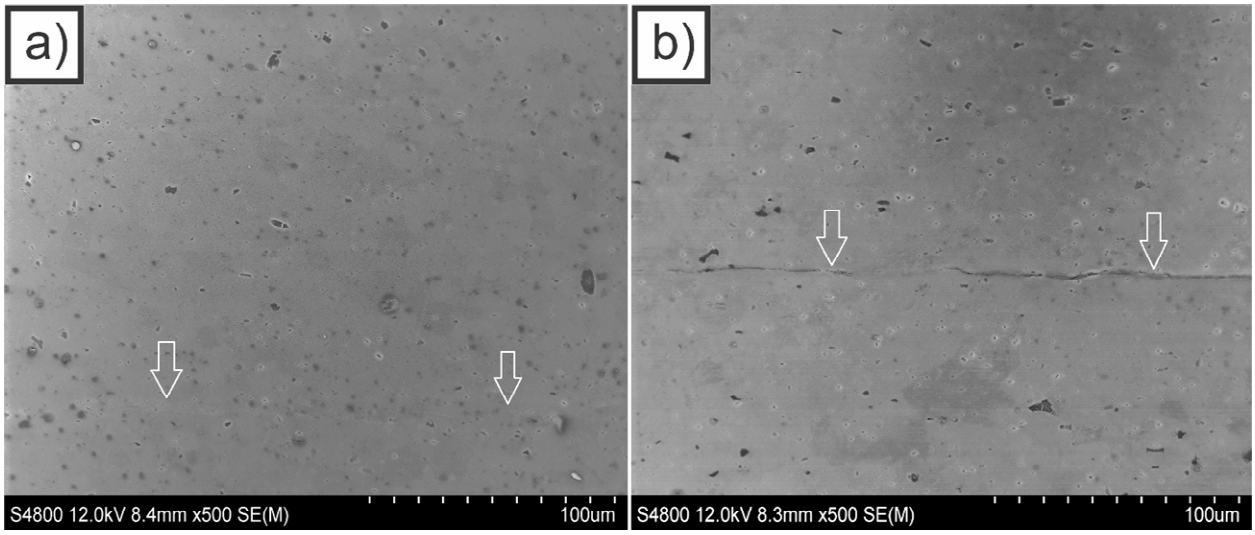

Fig. 17 SEM images of welded sheets joined at a rotational speed of 3500 RPM showing **(**a**)** welding interface between first and second sheet and (b) between second and third welding interface highlighting fully bonded and partially bonded regions

Conclusions

FSSW has remained one of the thrust areas in joining technology of manufacturing over the past few years. The two grand challenges identified from the extant literature addressed as part of this research are (i) FSSW of 0.3 mm thick sheets and (ii) FSSW of more than two thin sheets. By designing a novel pinless convex shaped tool, the paper reports achieving successful defect-less lap joining of a number of aluminium-magnesium (5754 H-111) sheets. During the course of this research, a couple of new scientific insights were gained about the FSSW process and following broad conclusions were obtained:

(i) Whilst using a convex shaped pin less tool, there is a trade-off for choosing the rotational speed responsible for the alteration of the microstructure. It was found that the applied strain rate (rotation speed of the tool) has a direct influence on the microstructure of the joined part i.e. low rotational speed leads to smaller grain sizes (grain refinement causinghigher microhardness of stir zone) and a higher rotation speed typically leading to an applied strain rate >400 s^{-1} leads to thermal softening.

(ii) The increase in microhardness of the FSSW was found to be accompanied by dominating effect of strain hardening, due to the competing mechanism of shear stress and axial stress present in the weld

zones. This competition leads to competing stick-slip mechanism until the onset of steady state weld conditions.

(iii) An increase in the rotational speed changes the d/D ratio causing a change of the weld pool profile from being cylindrical to conical. Also, it decreases the thickness of the welds in the center of the stir zone.

(iv) Until a certain threshold rotational speed, the quality of weld joint is better and did not show any defects and partially bonded regions, but higher speed arouses the possibility of developing defects in the stir zone. Weld interfaces showed uniform mechanical properties)hardness and modulus) regardless of the rotation speeds.

(v) Overall, the variation in the temperature in the FSSW process was seen to be relatively low when compared to the variation in the shear stress during the process. Consequently, it appears that the FSSW process is primarily driven by the presence and domination of the ratio of shear and axial stress making the FSSW process to be stress dominated rather than temperature dominated. Least to mention that the ratio of the two stresses directly refers to coefficient of friction and thus the name of the process being Friction stir welding is fully justified in this context.

Acknowledgements:

Authors are grateful to the DAAD program for the financial support to perform the work. Specific thanks to our collaboratiors Dr Vishal Panchal and Dr Stephen Lewandowski from Bruker, UK as well as support of the Henry Royce Institute for Ms Danka Labus Zlatanovic through the Royce PhD Equipment Access Scheme (Dr David Stanley) enabling access to TEM facilities at Royce@Cambridge via UKRI Grant EP/R00661X/1. We also express thanks to the STSM support from Cost Action CA15102 (funded by H2020). Additionally, SG is very much thankful to the Research support provided by the UKRI via Grants No.: (EP/K503241/1, EP/L016567/1, EP/S013652/1, EP/T001100/1, EP/S036180/1 and EP/T024607/1), H2020 (Cost Actions (CA18125, CA18224 and CA16235) and EURAMET EMPIR A185 (2018)), Royal Academy of Engineering Grant No. IAPP18-19\295 (Indo-

UK partnership), Royal Academy of Engineering Grant No. TSP1332 (South Africa- UK partnership) and Newton Fellowship award from the Royal Society (NIF\R1\191571). Also, computations calculation work performed on the Isambard Bristol, UK supercomputing service accessed by Resource Allocation Panel (RAP) grant is also acknowledged.

References:

1. Regensburg A, Petzoldt F, Benss T, Bergmann JP (2018) Liquid interlayer formation during friction stir spot welding of aluminum / copper. Weld World 63:117–125
2. Ojo OO, Taban E, Kaluc E (2015) Friction stir spot welding of aluminum alloys: A recent review. Mater Test 57:595–627
3. Lee WB, Yeon YM, Jung SB (2003) The improvement of mechanical properties of friction-stir-welded A356 Al alloy. Mater Sci Eng A 355:154–159. https://doi.org/10.1016/S0921-5093(03)00053-4
4. Manladan SM, Yusof F, Ramesh S, et al (2017) A review on resistance spot welding of aluminum alloys
5. Lei HY, Li YB, Carlson BE (2017) Cold metal transfer spot welding of 1 mm thick AA6061-T6. J Manuf Process 28:209–219. https://doi.org/10.1016/j.jmapro.2017.06.004
6. Hajavifard R, Motahari M, Özden H, et al (2016) The Effects of Pulse Shaping Variation in Laser Spot-Welding of Aluminum. Procedia Manuf 5:232–247. https://doi.org/10.1016/j.promfg.2016.08.021
7. Ni ZL, Ye FX (2018) Ultrasonic spot welding of aluminum alloys: A review. J Manuf Process 35:580–594. https://doi.org/10.1016/j.jmapro.2018.09.009
8. Li D, Chrysanthou A, Patel I, Williams G (2017) Self-piercing riveting-a review. Int J Adv Manuf Technol 92:1777–1824. https://doi.org/10.1007/s00170-017-0156-x
9. R.S. Mishra, Z.Y. Ma (2005) Friction stir welding and processing. Mater Sci Eng R 50 50:1–78. https://doi.org/10.1016/j.mser.2005.07.001
10. (2003) Mazda Develops World's First Steel and Aluminum Joining Technology Using Friction Heat. In: Maz. News Release. https://www2.mazda.com/en/publicity/release/2005/200506/050602.html. Accessed 26 Aug 2019
11. Andalib H, Farahani M, Enami M (2018) Study on the new friction stir spot weld joint reinforcement technique on 5754 aluminum alloy. Proc Inst Mech Eng Part C J Mech Eng Sci 232:2976–2986. https://doi.org/10.1177/0954406217729419
12. Piccini JM, Svoboda HG (2017) Tool geometry optimization in friction stir spot welding of Al-steel joints. J Manuf Process 26:142–154. https://doi.org/10.1016/j.jmapro.2017.02.004
13. Babu S, Sankar VS, Janaki Ram GD, et al (2013) Microstructures and mechanical properties of friction stir spot welded aluminum alloy AA2014. J Mater Eng Perform 22:71–84. https://doi.org/10.1007/s11665-012-0218-z
14. Yang XW, Fu T, Li WY (2014) Friction Stir Spot Welding : A Review on Joint Macro- and Microstructure , Property , and Process Modelling. Adv Mater Sci Eng 2014:1–11
15. Yazdi SR, Beidokhti B, Haddad-Sabzevar M (2019) Pinless tool for FSSW of AA 6061-T6

aluminum alloy. J Mater Process Technol 267:44–51. https://doi.org/10.1016/j.jmatprotec.2018.12.005

16. Uematsu Y, Tokaji K, Tozaki Y, et al (2008) Effect of re-filling probe hole on tensile failure and fatigue behaviour of friction stir spot welded joints in Al-Mg-Si alloy. Int J Fatigue 30:1956–1966. https://doi.org/10.1016/j.ijfatigue.2008.01.006

17. Li G, Zhou L, Luo L, et al (2019) Microstructural evolution and mechanical properties of refill friction stir spot welded alclad 2A12-T4 aluminum alloy. J Mater Res Technol 8:4115–4129. https://doi.org/10.1016/j.jmrt.2019.07.021

18. Fukada S, Ohashi R, Fujimoto M, Okada H (2013) Refill friction stir spot welding of dissimilar materials consisting of A6061 and hot dip zinc-coated steel sheets. In: Proceedings of the 1st International Joint Symposium on Joining and Welding. pp 183–187

19. Ding Y, Shen Z, Gerlich AP (2017) Refill friction stir spot welding of dissimilar aluminum alloy and AlSi coated steel. J Manuf Process 30:353–360. https://doi.org/10.1016/j.jmapro.2017.10.006

20. Xu Z, Li Z, Ji S, Zhang L (2018) Refill friction stir spot welding of 5083-O aluminum alloy. J Mater Sci Technol 34:878–885. https://doi.org/10.1016/j.jmst.2017.02.011

21. Cao JY, Wang M, Kong L, et al (2014) Microstructure, texture and mechanical properties during refill friction stir spot welding of 6061-T6 alloy. Mater Charact J 128:54–62. https://doi.org/10.1016/j.matchar.2017.03.023

22. Ibrahim IJ, Yapici GG (2018) Application of a novel friction stir spot welding process on dissimilar aluminum joints. J Manuf Process 35:282–288. https://doi.org/10.1016/j.jmapro.2018.08.018

23. Li W, Li J, Zhang Z, et al (2014) Improving mechanical properties of pinless friction stir spot welded joints by eliminating hook defect. Mater Des 62:247–254. https://doi.org/10.1016/j.matdes.2014.05.028

24. Zhao YQ, Liu HJ, Chen SX, et al (2014) Effects of sleeve plunge depth on microstructures and mechanical properties of friction spot welded alclad 7B04-T74 aluminum alloy. Mater Des 62:40–46. https://doi.org/10.1016/j.matdes.2014.05.012

25. Bakavos D, Chen Y, Babout L, Prangnell P (2011) Material interactions in a novel pinless tool approach to friction stir spot welding thin aluminum sheet. Metall Mater Trans A Phys Metall Mater Sci 42:1266–1282. https://doi.org/10.1007/s11661-010-0514-x

26. Roos A (2010) Basic investigation about a new joining process called HFDB (Hybrid Friction Diffusion Bonding). TU Ilmenau, Germany

27. Kalpakijan S (1991) Manufacturing Processes for Engineering Materials. Addison Wesley Publishing Company

28. Benham PP, Crawford RJ, Armstrong CG (1996) Mechanics of Engineering Materials

29. Reilly A, Shercliff H, Chen Y, Prangnell P (2015) Modelling and visualisation of material flow in friction stir spot welding. J Mater Process Technol 225:473–484. https://doi.org/10.1016/j.jmatprotec.2015.06.021

30. Farhat ZN, Ding Y, Northwood DO, Alpas AT (1996) Effect of grain size on friction and wear of nanocrystalline aluminum. Mater Sci Eng A 206:302–313

31. Kumar K, Kalyan C, Kailas S V, et al (2009) An Investigation of Friction During Friction Stir Welding of Metallic Materials An Investigation of Friction During Friction Stir Welding. Mater Manuf Process 24:438–445. https://doi.org/10.1080/10426910802714340

32. Yamada H, Kami T, Mori R, et al (2018) Strain rate dependence of material strength in aa5xxx series aluminum alloys and evaluation of their constitutive equation. Metals (Basel) 8:1–15. https://doi.org/10.3390/met8080576

33. Chang CI, Lee CJ, Huang JC (2004) Relationship between grain size and Zener-Holloman parameter during friction stir processing in AZ31 Mg alloys. Scr Mater 51:509–514. https://doi.org/10.1016/j.scriptamat.2004.05.043

34. Gerlich A, Yamamoto M, North TH (2007) Strain rates and grain growth in Al 5754 and Al 6061 friction stir spot welds. Metall Mater Trans A Phys Metall Mater Sci 38:1291–1302. https://doi.org/10.1007/s11661-007-9155-0

35. Jata K V, Semiatin SL (2000) Continuous dynamic recrystallization during friction stir welding of high strength aluminum alloys. Scr Mater 43:743–749

36. Gerlich A, Su P, Yamamoto M, North TH (2007) Effect of welding parameters on the strain rate and microstructure of friction stir spot welded 2024 aluminum alloy. J Mater Sci 42:5589–5601. https://doi.org/10.1007/s10853-006-1103-7

37. Bagheri B, Abbasi M, Abdollahzadeh A, Omidvar H (2019) Advanced Approach to Modify Friction Stir Spot Welding Process. Met Mater Int. https://doi.org/10.1007/s12540-019-00416-x

38. Wei S, Liu Y, Liu X, Zhao H (2019) Investigation on edge chipping evaluation of Si 3 N 4 ceramics milling surface. Meas J Int Meas Confed 133:241–250. https://doi.org/10.1016/j.measurement.2018.10.015

39. Shen Z, Yang X, Zhang Z, et al (2013) Microstructure and failure mechanisms of refill friction stir spot welded 7075-T6 aluminum alloy joints. Mater Des 44:476–486. https://doi.org/10.1016/j.matdes.2012.08.026

40. Badarinarayan H, Yang Q, Zhu S (2009) Effect of tool geometry on static strength of friction stir spot-welded aluminum alloy. Int J Mach Tools Manuf 49:142–148. https://doi.org/10.1016/j.ijmachtools.2008.09.004

41. Ruzek R, Kadlec M (2014) Friction stir welded structures : Kissing bond defects. Int J Terrasp Sci Eng 6:77–83